

On the Influence of Ferroelectric Polarization States on the Magneto-electric Coupling in Two-phase Composites

M. Labusch, M.-A. Keip, V.V. Shvartsman, D.C. Lupascu, J. Schröder

Of particular attention in a variety of novel technical applications is the coupling between magnetic and electric field quantities. Materials that show magneto-electric (ME) coupling could enable new smart devices in the area of electric-field-controlled magnetic-data storage or highly sensitive magnetic-field sensors. In general, ME materials exhibit both a spontaneous magnetization and a spontaneous polarization. In this respect, they feature two ferroic states at the same time and are thus termed magneto-electric multiferroics. However, all natural and most of the synthesized ME multiferroics do not show an interaction between magnetization and electric polarization in the technically relevant temperature range. Thus, there is need for alternative realizations for ME coupling materials. A promising idea lies in the design and manufacturing of ME composites. These materials consist of a magnetostrictive and a piezoelectric phase and generate the ME coupling as a strain-induced product property. Since there exists a wealth of stable magnetostrictive and piezoelectric materials at ambient temperature, such composites yield the desired ME coupling also in a technically useful temperature range. In any case, the effective ME coupling is driven by microscopic interactions between the individual phases and thus highly depends on the microstructure of the composite. This calls for powerful homogenization methods that are able to predict the effective coupling for arbitrary microstructural morphologies. Motivated by that, we apply a two-scale computational homogenization framework for magneto-electro-mechanically coupled boundary value problems, which allows us to analyze the ME composite structures and calculate the effective ME-coefficient. Furthermore, by using a non-linear ferroelectric material model on the micro-level, we are able to simulate the polarization process of the ferroelectric phase. We show that this has a significant impact on the obtainable ME-coefficient.

1 Introduction

Materials with ferroelectric or ferromagnetic properties are used in many fields of technology. A combination of both properties in a single material, enable new applications such as electrical magnetic-field sensors or electric-write/magnetic-read memories, see for example Eerenstein et al. (2006), Spaldin and Fiebig (2005) and Bibes and Barthélémy (2008). Such materials, which combine polarization and magnetization, are known as *magneto-electric (ME) multiferroics*. However, all natural and most of the synthetic single-phase ME multiferroics show ME coupling only outside a technical useful temperature range, see Table 1 for an overview of measured ME coefficients.

Table 1: Measured ME coefficients of single-phase materials.

Material	ME coefficient	Temperature	Reference
LiCoPO ₄	$30.60 \cdot 10^{-12}$ s/m	4.2 K	Rivera (1994)
Cr ₂ O ₃	$4.17 \cdot 10^{-12}$ s/m	270.0 K	Vaz et al. (2010)
Cr ₂ O ₃	$4.13 \cdot 10^{-12}$ s/m	263.0 K	Rivera (1994)
Cr ₂ O ₃	$1.43 \cdot 10^{-12}$ s/m	293.2 K	Astrov (1961)
BiFeO ₃	$0.52 \cdot 10^{-12}$ s/m	18.0 K	Rivera and Schmid (1997)
Mn ₃ B ₇ O ₁₃ I	$9.50 \cdot 10^{-14}$ s/m	4.2 K	Crottaz et al. (1997)

The disadvantage of a vanishing ME coupling coefficient at room temperature, which is not feasible for technical applications, could be circumvented by manufacturing magneto-electric composites, which consist of a piezoelectric and a magnetostrictive phase, see Nan (1994); Fiebig (2005) and Hill (2000). In such composites, the individual phases interact with one another mechanically, so that a *strain-induced* ME coupling (even at ambient temperature) can be produced. The resulting effective ME couplings, which are not present in each of the constituents,

are classified as *product properties*. We distinguish between the direct and the inverse ME effect. The direct coupling effect characterizes magnetically induced polarization: an applied magnetic field yields a deformation of the magneto-active phase which is transferred to the electro-active phase. As a result, a strain-induced polarization in the electro-active phase is observed, see Figure 1. The converse effect is characterized by an electric-field induced magnetization. Several experiments on ME composites showed remarkable ME coefficients, which are orders of magnitudes higher than those of single-phase multiferroics, see, for example, Fiebig (2005).

Due to the microscopic interactions between the individual phases, the arising ME coefficient strongly depends on the microstructure of the composite. Motivated by that, we recapitulate a two-scale finite element homogenization framework (FE²-method) for magneto-electro-mechanically coupled boundary value problems, see Schröder et al. (2015a). This allows for the consideration of microscopic morphologies in a macroscopic simulation. In the context of multiscale homogenization we refer to Miehe and Koch (2002), Miehe and Bayreuther (2007), Geers et al. (2010) as well as to recent extensions to coupled material response Miehe et al. (2011), Schröder and Keip (2012), Zäh and Miehe (2013), Labusch et al. (2014), Keip et al. (2014) or Schröder et al. (2015b).

Obviously, the polarization state of the ferroelectric phase strongly influences the ME coupling. The reason for that is that in a bulk composite the electro-mechanical coupling of the ferroelectric phase has to be poled in order to allow for significant strain-induced interactions. The pre-polarization is thus crucial in the manufacturing and the design of ME composites. At this point we want to refer to Avakian et al. (2015), where the authors used a non-linear ferroelectric model to simulate the magneto-electric coupling in composite materials regarding the polarization of the electric matrix. In order to map this in our simulations, we consider a non-linear hysteretic material model for the ferroelectric phase on the microscopic level. This non-linear model is based on a microscopic switching criterion for the spontaneous polarization based on the work of Hwang et al. (1995). The material model will be combined with a magneto-electric enthalpy function which reflects the tetragonal symmetry of a barium titanate unit cell, compare to Keip and Schröder (2011); Keip and Schröder (2011) or Keip (2012).

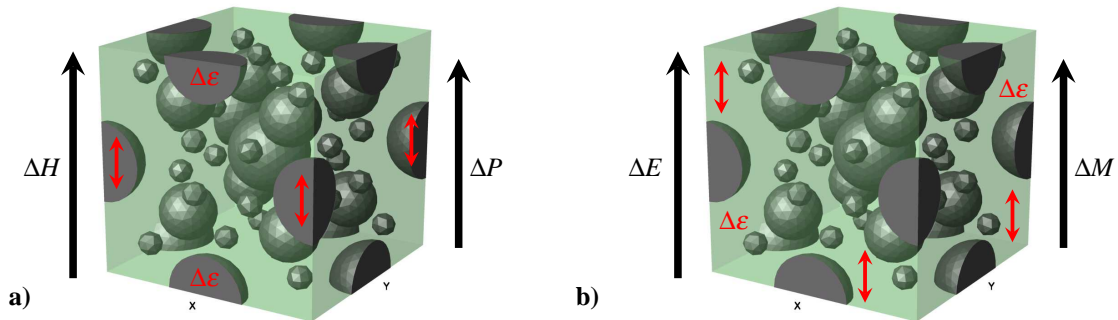


Figure 1: a) Direct coupling effect and b) inverse coupling effect, see Schröder et al. (2015a).

The outline of this contribution is as follows. In the second section, the main ingredients of the coupled finite element homogenization approach will be discussed briefly. We further describe the used non-linear material model reflecting the ferroelectric switching behavior. Section three then gives a numerical example, in which the influence of the microscopic switching behavior on obtainable ME-coefficients is analyzed. The results will be compared to experimental measurements. In section four a conclusion is given.

2 Multiscale Homogenization of ME Composites

In this section the two-scale homogenization framework for magneto-electro-mechanically coupled boundary value problems will be described briefly. We start with the definition of the kinematic quantities and the fundamental balance equations on the macroscale. The connection to the microscale is established by a localization step. The subsequent homogenization step yields the effective properties including the desired ME coefficient. After that, the used material models on the microscopic level will be described. We employ a linear and transversely isotropic material model for the magneto-active phase and a non-linear hysteretic model for the electro-active phase. In order to simplify the readability of this section we summarize the basic magneto-electro-mechanical quantities in Table 2. All macroscopic quantities are denoted by an overline.

Table 2: Magneto-electro-mechanical quantities and their units.

micro- and macro-Symbol	Continuum mechanical description	SI-Unit
u, \bar{u}	displacement vector	m
$\varepsilon, \bar{\varepsilon}$	linear strain tensor	1
$\sigma, \bar{\sigma}$	Cauchy strain tensor	kg/s ² m (N/m ²)
t, \bar{t}	traction vector	kg/s ² m (N/m ²)
f, \bar{f}	mechanical body forces	kg/s ² m ² (N/m ³)
$\phi, \bar{\phi}$	electric potential	kg m ² /A s ³ (V)
E, \bar{E}	electric field vector	kg m/A s ³ (V/m)
D, \bar{D}	electric displacement vector	A s/m ² (C/m ²)
Q, \bar{Q}	electric surface flux density	A s/m ² (C/m ²)
q, \bar{q}	density of free charge carriers	A s/m ³ (C/m ³)
$\varphi, \bar{\varphi}$	magnetic potential	A
H, \bar{H}	magnetic field	A/m
B, \bar{B}	magnetic flux density	kg/A s ² (T)
$\zeta, \bar{\zeta}$	magnetic surface flux density	kg/A s ² (Vs/m ²)

2.1 Boundary Value Problems and Scale Transition

The macroscopic body $\mathcal{B} \subset \mathbb{R}^3$ is parameterized in the Cartesian coordinates \bar{x} . The macroscopic fundamental balance laws are given by the balance of momentum as well as Gauß's laws of electro- and magneto-statics

$$\operatorname{div}_{\bar{x}}[\bar{\sigma}] + \bar{f} = 0, \quad \operatorname{div}_{\bar{x}}[\bar{D}] = \bar{q} \quad \text{and} \quad \operatorname{div}_{\bar{x}}[\bar{B}] = 0 \quad \text{in } \mathcal{B}. \quad (1)$$

The macroscopic gradient fields, i.e. the strain as well as the electric and magnetic field are defined as

$$\bar{\varepsilon}(\bar{x}) := \operatorname{sym}[\bar{\nabla} \bar{u}(\bar{x})], \quad \bar{E}(\bar{x}) := -\bar{\nabla} \bar{\phi}(\bar{x}) \quad \text{and} \quad \bar{H}(\bar{x}) := -\bar{\nabla} \bar{\varphi}(\bar{x}), \quad (2)$$

with the macroscopic gradient operator $\bar{\nabla}$ with respect to \bar{x} . The boundary conditions prescribed through the displacement and the surface traction

$$\bar{u} = \bar{u}_0 \quad \text{on } \partial \mathcal{B}_u \quad \text{and} \quad \bar{t}_0 = \bar{\sigma} \cdot \bar{n} \quad \text{on } \partial \mathcal{B}_\sigma \quad \text{with} \quad \partial \mathcal{B}_u \cup \partial \mathcal{B}_\sigma = \partial \mathcal{B} \quad \text{and} \quad \partial \mathcal{B}_u \cap \partial \mathcal{B}_\sigma = \emptyset \quad (3)$$

the electric potential and the electric surface flux density

$$\bar{\phi} = \bar{\phi}_0 \quad \text{on } \partial \mathcal{B}_\phi \quad \text{and} \quad -\bar{Q}_0 = \bar{D} \cdot \bar{n} \quad \text{on } \partial \mathcal{B}_D \quad \text{with} \quad \partial \mathcal{B}_\phi \cup \partial \mathcal{B}_D = \partial \mathcal{B} \quad \text{and} \quad \partial \mathcal{B}_\phi \cap \partial \mathcal{B}_D = \emptyset \quad (4)$$

as well as through the magnetic potential and the magnetic surface flux density

$$\bar{\varphi} = \bar{\varphi}_0 \quad \text{on } \partial \mathcal{B}_\varphi \quad \text{and} \quad -\bar{\zeta}_0 = \bar{B} \cdot \bar{n} \quad \text{on } \partial \mathcal{B}_B \quad \text{with} \quad \partial \mathcal{B}_\varphi \cup \partial \mathcal{B}_B = \partial \mathcal{B} \quad \text{and} \quad \partial \mathcal{B}_\varphi \cap \partial \mathcal{B}_B = \emptyset. \quad (5)$$

In a two-scale simulation, we attach a representative volume element $\mathcal{RVE} \subset \mathbb{R}^3$ at each macroscopic point. As a consequence, all the above quantities are defined through an averaging process over the volume of the \mathcal{RVE} . Assuming continuity of the displacements as well as the electric and magnetic potential, we can express the macroscopic variables in terms of simple volume integrals as

$$\bar{\xi} = \langle \xi \rangle_V := \frac{1}{V_{\mathcal{RVE}}} \int_{\mathcal{RVE}} \xi \, dv \quad \text{with} \quad \xi := \{\varepsilon, \sigma, E, D, H, B\}, \quad (6)$$

see, for example, Schröder et al. (2015a).

The microscopic boundary value problem is defined as follows. The balance of momentum as well as Gauß's law of electro- and magneto-statics are given by

$$\operatorname{div}_x[\sigma] = 0, \quad \operatorname{div}_x[D] = q \quad \text{and} \quad \operatorname{div}_x[B] = 0 \quad \text{in } \mathcal{RVE}. \quad (7)$$

The linear strains as well as the microscopic electric and magnetic fields are defined by

$$\varepsilon(x) := \operatorname{sym}[\nabla u(x)], \quad E(x) := -\nabla \phi(x) \quad \text{and} \quad H(x) := -\nabla \varphi(x). \quad (8)$$

For the complete definition of the microscopic boundary value problem, we need to prescribe suitable boundary conditions on the $\mathcal{R}\mathcal{V}\mathcal{E}$. Starting from the fundamental works of Hill (1963) and Mandel and Dantu (1963) we assume that the individual parts of a generalized magneto-electro-mechanical Hill-Mandel condition of the form

$$\bar{\sigma} : \dot{\bar{\varepsilon}} = \langle \sigma : \dot{\varepsilon} \rangle_V, \quad \bar{D} \cdot \dot{\bar{E}} = \langle D \cdot \dot{E} \rangle_V \quad \text{and} \quad \bar{B} \cdot \dot{\bar{H}} = \langle B \cdot \dot{H} \rangle_V \quad (9)$$

have to be fulfilled independently, see Schröder (2009) for the electro-mechanical case and Schröder et al. (2015a) for the magneto-electro-mechanical case. In order to satisfy these conditions, we employ periodic boundary conditions in such a way that we assume a decomposition of the microscopic strains as well as the electric and magnetic field into a macroscopic part and a fluctuation part, satisfying $\langle \xi \rangle_V = \bar{\xi}$ and $\langle \tilde{\xi} \rangle_V = 0$, as

$$\varepsilon = \bar{\varepsilon} + \tilde{\varepsilon}, \quad E = \bar{E} + \tilde{E} \quad \text{and} \quad H = \bar{H} + \tilde{H}. \quad (10)$$

The associated periodic boundary conditions for the mechanical, electrical and magnetical part are then given by

$$\begin{aligned} \tilde{u}(x^+) &= \tilde{u}(x^-) \quad \text{and} \quad t(x^+) = -t(x^-), \\ \tilde{\phi}(x^+) &= \tilde{\phi}(x^-) \quad \text{and} \quad Q(x^+) = -Q(x^-), \\ \tilde{\varphi}(x^+) &= \tilde{\varphi}(x^-) \quad \text{and} \quad \zeta(x^+) = -\zeta(x^-), \end{aligned} \quad (11)$$

respectively.

2.2 Consistent Linearization

In order to obtain a quadratic convergence in a Newton-Raphson iteration scheme on both scales, a consistent linearization of the macroscopic constitutive quantities is required. The incremental constitutive equations on the macroscopic and microscopic level can be written down as

$$\begin{bmatrix} \Delta \bar{\sigma} \\ -\Delta \bar{D} \\ -\Delta \bar{B} \end{bmatrix} = \begin{bmatrix} \bar{\mathbb{C}} & -\bar{e}^T & -\bar{q}^T \\ -\bar{e} & -\bar{\epsilon} & -\bar{\alpha}^T \\ -\bar{q} & -\bar{\alpha} & -\bar{\mu} \end{bmatrix} \begin{bmatrix} \Delta \bar{\varepsilon} \\ \Delta \bar{E} \\ \Delta \bar{H} \end{bmatrix} \quad \text{and} \quad \begin{bmatrix} \Delta \sigma \\ -\Delta D \\ -\Delta B \end{bmatrix} = \begin{bmatrix} \mathbb{C} & -e^T & -q^T \\ -e & -\epsilon & -\alpha^T \\ -q & -\alpha & -\mu \end{bmatrix} \begin{bmatrix} \Delta \varepsilon \\ \Delta E \\ \Delta H \end{bmatrix} \quad (12)$$

with the macroscopic and microscopic elasticity tangent modulus $\bar{\mathbb{C}}$ and \mathbb{C} , the piezoelectric tangent moduli \bar{e} and e , the piezomagnetic tangent moduli \bar{q} and q , the electric permittivities $\bar{\epsilon}$ and ϵ , the magnetic permeabilities $\bar{\mu}$ and μ , as well as the magneto-electric tangent moduli $\bar{\alpha}$ and α . The microscopic constitutive moduli are defined as partial derivatives of the stresses, the electric displacement and the magnetic induction with respect to the microscopic strains as well as electric and magnetic field as

$$\mathbb{C} = \partial_\varepsilon \sigma, \quad \epsilon = \partial_E D, \quad \mu = \partial_H B, \quad e = \partial_\varepsilon D = -(\partial_E \sigma)^T, \quad q = \partial_E B = -(\partial_H \sigma)^T \quad \text{and} \quad \alpha = \partial_E B = (\partial_H D)^T \quad (13)$$

For the determination of the macroscopic constitutive tangent moduli the macroscopic stresses, electric displacement and magnetic induction are expressed by the volume averages of the corresponding microscopic variables

$$\begin{aligned} \bar{\mathbb{C}} &= \frac{\partial \langle \sigma \rangle_V}{\partial \bar{\varepsilon}}, \quad \bar{\epsilon} = \frac{\partial \langle D \rangle_V}{\partial \bar{E}}, \quad \bar{\mu} = \frac{\partial \langle B \rangle_V}{\partial \bar{H}}, \\ \bar{e} &= \frac{\partial \langle D \rangle_V}{\partial \bar{\varepsilon}} = \left[-\frac{\partial \langle \sigma \rangle_V}{\partial \bar{E}} \right]^T, \quad \bar{q} = \frac{\partial \langle B \rangle_V}{\partial \bar{\varepsilon}} = \left[-\frac{\partial \langle \sigma \rangle_V}{\partial \bar{H}} \right]^T, \\ \bar{\alpha} &= \frac{\partial \langle B \rangle_V}{\partial \bar{E}} = \left[\frac{\partial \langle D \rangle_V}{\partial \bar{H}} \right]^T. \end{aligned} \quad (14)$$

For a detailed derivative of the effective tangent moduli for magneto-electro-mechanically coupled material response we refer to Schröder et al. (2015a). Although the ME coefficients α of the microscopic constituents are zero, the macroscopic coefficients in $\bar{\alpha}$ are generally non-zero.

2.3 Transversely Isotropic Material Model

On the microscopic level we describe the behavior of a piezomagnetic and a non-linear ferroelectric phase. The piezomagnetic phase is modeled with a transversely isotropic material law in terms of a coordinate-invariant

magneto-electro-mechanical enthalpy function adopted from the work of Schröder and Gross (2004). It is given by

$$\psi_1 = \psi_1^{mech} + \psi_1^{pe} + \psi_1^{pm} + \psi_1^{diel} + \psi_1^{magn} \quad (15)$$

where the individual parts represent the mechanical, piezoelectric, piezomagnetic, dielectric and magnetic behavior. They are defined as

$$\begin{aligned} \psi_1^{mech} &= \frac{1}{2}\lambda I_1^2 + \mu I_2 + \omega_1 I_5 + \omega_2 I_4^2 + \omega_3 I_1 I_4, \\ \psi_1^{pe} &= \beta_1 I_1 J_2^e + \beta_2 I_4 J_2^e + \beta_3 K_1^e, \\ \psi_1^{pm} &= \kappa_1 I_1 J_2^m + \kappa_2 I_4 J_2^m + \kappa_3 K_1^m, \\ \psi_1^{diel} &= \gamma_1 J_1^e + \gamma_2 (J_2^e)^2, \\ \psi_1^{magn} &= \xi_1 J_1^m + \xi_2 (J_2^m)^2, \end{aligned} \quad (16)$$

with the material parameters $\lambda, \mu, \omega_{1-3}, \beta_{1-3}, \kappa_{1-3}, \gamma_{1-2}$, and ξ_{1-2} . Above, we used the invariants

$$\begin{aligned} I_1 &:= \text{tr}[\boldsymbol{\varepsilon}], \quad I_2 := \text{tr}[\boldsymbol{\varepsilon}^2], \quad I_4 := \text{tr}[\boldsymbol{\varepsilon} \boldsymbol{m}], \quad I_5 := \text{tr}[\boldsymbol{\varepsilon}^2 \boldsymbol{m}], \\ J_1^e &:= \text{tr}[E \otimes E], \quad J_2^e := \text{tr}[E \otimes a], \quad K_1^e := \text{tr}[\boldsymbol{\varepsilon} \cdot (E \otimes a)], \\ J_1^m &:= \text{tr}[H \otimes H], \quad J_2^m := \text{tr}[H \otimes a], \quad K_1^m := \text{tr}[\boldsymbol{\varepsilon} \cdot (H \otimes a)], \end{aligned} \quad (17)$$

defined in terms of the preferred direction a , which characterizes the axis normal to the plane of isotropy, and the associated material tensor $m = a \otimes a$ with $\|a\| = 1$. The preferred direction is associated with the direction of remanent magnetization of the piezomagnetic phase. Note that for the description of the piezomagnetic phase, we neglected the piezoelectric part ψ_1^{pe} and for the description of the piezoelectric phase in chapter 3.4 we neglected the piezomagnetic part ψ_1^{pm} .

2.4 Ferroelectric/-elastic switching Behavior

The non-linear hysteretic response of the ferroelectric phase will be modeled through a microscopic switching criterion for the remanent polarization based on the work of Hwang et al. (1995). A wealth of models has been developed, which range from approaches on the basis of classical plasticity theory (McMeeking and Landis (2002); Kamlah et al. (2005); Miehe and Rosato (2011)), models inspired by crystal plasticity (Huber et al. (1999); Schröder and Romanowski (2005); Klinkel (2006)), phase-field models (Zhang and Bhattacharya (2005); Schrade et al. (2007, 2014)) and purely microscopic approaches (Hwang et al. (1995); McMeeking and Hwang (1997); Kessler and Balke (2001); Li et al. (2010)). The used material model for the electro-active phase is adopted from the work of Hwang et al. (1995) and reflects the hysteretic ferroelectric response of tetragonal Barium Titanate. We start with writing down the magneto-electro-mechanical enthalpy function, based on the works of Keip and Schröder (2011) and Keip and Schröder (2011)

$$\psi_2 = \psi_2^{mech} + \psi_2^{pe} + \psi_2^{diel} + \psi_2^{magn} \quad (18)$$

with the individual parts, whereas (\bullet) denotes the property on barium titanate unit cell level,

$$\begin{aligned} \psi_2^{mech} &= \frac{1}{2}\lambda \hat{I}_1^2 + \mu \hat{I}_2 + \frac{1}{2}\omega_1 \hat{I}_5^2 + \omega_2 \hat{I}_1 \hat{I}_5 + \frac{1}{2}\omega_3 (\hat{I}_6^2 + \hat{I}_7^2) + \frac{1}{2}\omega_4 (\hat{I}_3^2 + \hat{I}_4^2 + \hat{I}_5^2), \\ \psi_2^{pe} &= \beta_1 \hat{K}_1 + \beta_2 \hat{I}_1 \hat{J}_2^e + \beta_3 \hat{I}_5 \hat{J}_2^e, \\ \psi_2^{diel} &= \frac{1}{2}\gamma_1 \hat{J}_1^e + \frac{1}{2}(\gamma_2 - \gamma_1) (\hat{J}_2^e)^2 - \hat{J}_2^e \hat{P}_1, \\ \psi_2^{magn} &= \frac{1}{2}\xi_1 \hat{J}_1^m + \frac{1}{2}(\xi_2 - \xi_1) (\hat{J}_2^m)^2. \end{aligned} \quad (19)$$

The above parts of the enthalpy function are described with the invariants

$$\begin{aligned} \hat{I}_1 &= \text{tr}[\hat{\boldsymbol{\varepsilon}}^e], \quad \hat{I}_2 = \text{tr}[(\hat{\boldsymbol{\varepsilon}}^e)^2], \quad \hat{I}_3 = \text{tr}[\hat{\boldsymbol{\varepsilon}}^e \hat{\boldsymbol{M}}_{11}], \quad \hat{I}_4 = \text{tr}[\hat{\boldsymbol{\varepsilon}}^e \hat{\boldsymbol{M}}_{22}], \quad \hat{I}_5 = \text{tr}[\hat{\boldsymbol{\varepsilon}}^e \hat{\boldsymbol{M}}_{33}], \\ \hat{I}_6 &= \text{tr}[\hat{\boldsymbol{\varepsilon}}^e \hat{\boldsymbol{\varepsilon}}_1], \quad \hat{I}_7 = \text{tr}[\hat{\boldsymbol{\varepsilon}}^e \hat{\boldsymbol{\varepsilon}}_2], \quad \hat{J}_1^e = \text{tr}[E \otimes E], \quad \hat{J}_1^m = \text{tr}[H \otimes H], \\ \hat{J}_2^e &= \text{tr}[E \otimes \hat{c}], \quad \hat{J}_2^m = \text{tr}[H \otimes \hat{c}], \quad \hat{K}_1 = \text{tr}[E \otimes (\hat{\boldsymbol{\varepsilon}}_3 : \hat{\boldsymbol{\varepsilon}}^e)], \quad \hat{P}_1 = \text{tr}[\hat{\boldsymbol{P}}^r \otimes \hat{c}]. \end{aligned} \quad (20)$$

Here, we have introduced a set of structural tensors based on the crystallographic axes \hat{a}_1, \hat{a}_2 , and \hat{a}_3 given by

$$\hat{\boldsymbol{M}}_{ij} = \hat{a}_i \otimes \hat{a}_j, \quad \hat{\boldsymbol{\varepsilon}}_1 = (\hat{\boldsymbol{M}}_{13} + \hat{\boldsymbol{M}}_{31}), \quad \hat{\boldsymbol{\varepsilon}}_2 = (\hat{\boldsymbol{M}}_{23} + \hat{\boldsymbol{M}}_{32}), \quad \text{and} \quad \hat{\boldsymbol{\varepsilon}}_3 = \sum_{i=1}^3 (\hat{a}_i \otimes \hat{a}_i \otimes \hat{c} + \hat{a}_i \otimes \hat{c} \otimes \hat{a}_i). \quad (21)$$

In contrast to the piezomagnetic model the invariants of ψ_2 depend on the elastic strains, where we assume an additive decomposition of the total strains into a reversible (elastic) and an irreversible (remanent) part. In the same way, we subdivide the electric displacement, see for example Kamlah (2001), and obtain

$$\hat{\varepsilon} = \hat{\varepsilon}^e + \hat{\varepsilon}^r \quad \text{and} \quad \hat{D} = \hat{D}^e + \hat{P}^r. \quad (22)$$

The remanent strain $\hat{\varepsilon}^r$ and the remanent polarization \hat{P}^r are defined as functions of the preferred direction of a Barium Titanate unit cell $\hat{c} = \hat{a}_3$ as

$$\hat{\varepsilon}^r = \frac{3}{2} \hat{\varepsilon}_s \text{dev}(\hat{c} \otimes \hat{c}) \quad \text{and} \quad \hat{P}^r = \hat{P}_s \hat{c}. \quad (23)$$

where $\hat{\varepsilon}_s$ and \hat{P}_s are the spontaneous strain and spontaneous polarization. Each of these unit cells is allowed to perform 90° and 180° switching, see Figure 2, which illustrates possible 90° and 180° ferroelectric/-elastic switching options.

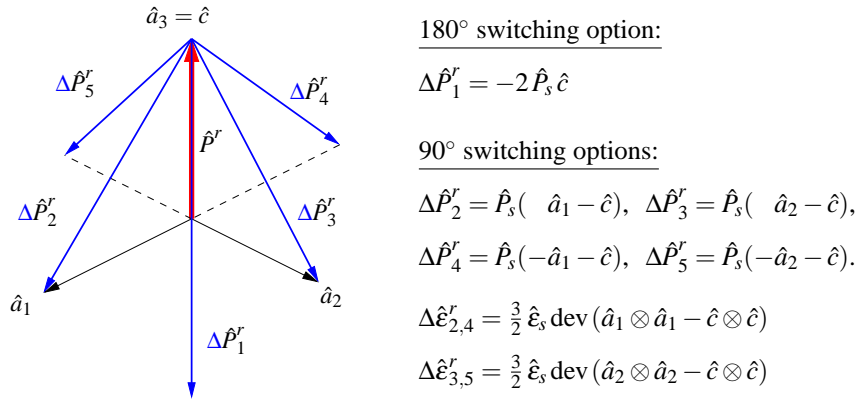


Figure 2: 180° and 90° switching options in tetragonal unit cell. The spontaneous polarization of the unit cell is given by $\hat{P}^r = \hat{P}_s \hat{c}$.

In order to represent the non-linear hysteretic behavior of a ferroelectric polycrystal, we assume a specific number of unit cell orientations in each microscopic integration point. This distribution should in simplified terms represent orientation directions of the unit cells in different domains, whereas concrete domain structures and domain wall movements as well as grain boundary effects are not taken into account. For a consideration of grain boundary conditions we want to refer to Arockiarajan et al. (2010). At the beginning of the simulation, we arrange them uniformly in the three-dimensional space. For the ferroelectric switching a corresponding criterion is adopted from the fundamental work of Hwang et al. (1995). Similarly, a criterion for the ferroelastic switching can be derived, which depends on the change of the spontaneous strains caused by an applied mechanical load, see Keip (2012). Due to different switching thresholds, the combined criterion for ferroelectric/-elastic switching is defined as

$$\frac{E \cdot \Delta \hat{P}_1^r}{\mathcal{W}_{e,180^\circ}^{\text{diss}}} \geq 1 \quad \text{and} \quad \frac{E \cdot \Delta \hat{P}_i^r}{\mathcal{W}_{e,90^\circ}^{\text{diss}}} + \frac{\sigma : \Delta \hat{\varepsilon}_i^r}{\mathcal{W}_{m,90^\circ}^{\text{diss}}} \geq 1 \quad \text{for } i = 2, \dots, 5. \quad (24)$$

with the work dissipated during a discrete switching process

$$\mathcal{W}_{e,180^\circ}^{\text{diss}} = 2 \hat{P}_s \hat{E}_c, \quad \mathcal{W}_{e,90^\circ}^{\text{diss}} = \hat{P}_s \hat{E}_c \quad \text{and} \quad \mathcal{W}_{m,90^\circ}^{\text{diss}} = \frac{3}{2} \hat{\varepsilon}_s \hat{\sigma}_c. \quad (25)$$

Here, \hat{E}_c and $\hat{\sigma}_c$ are the coercive electric field and stress, respectively. The switching process implicates a reorientation of the crystallographic lattice, such that a homogenization approach over the unit cell distributions in each microscopic integration point is necessary. The resulting microscopic quantities σ , D , \mathbb{C} , e and ϵ are based on n orientations and determined as

$$(\bullet) = \frac{1}{n} \sum_{i=1}^n (\bullet)_i, \quad (26)$$

After the homogenization process over the unit cells, the switching criterion is verified in each microscopic integration point and the algorithm is repeated until the unit cell orientations have adjusted without further fulfillment of the switching criterion.

3 Numerical Examples

In the following section we discuss numerical simulations of the applied homogenization method. First, we consider the macroscopic response of a ferroelectric bulk material by using different numbers of orientations, representing single barium titanate unit cells, in each microscopic gauss point. Then, a mechanical force is applied in the same direction as the alternating electric field to demonstrate the pressure dependence of the ferroelectric model and the enhancement of the electro-mechanical coupling. Both investigations are used to perform pressure dependent simulations on a magneto-electric composite, where a specific number of orientations is chosen for the ferroelectric matrix. The resulting ME-coefficients are discussed with respect to the ferroelectric polarization state and the applied compressive stresses. Next to the pre-polarization state, the microscopic morphology of the composite plays a prominent role for the ME-coefficient. To show such an influence we finally performed multiple simulations with different inclusion geometries and volume fractions. In these simulations we restrict the calculations to two-dimensional microstructures and purely linear material models for both constituents.

3.1 Ferroelectric Response of Different Orientation Distributions

In order to investigate the material response of a ferroelectric single-phase material, we performed simulations with different numbers of attached orientations in each microscopic gauss point, which represent barium titanate unit cells. The set of material parameters used to describe tetragonal barium titanate is listed in Table 3. Depending on the permittivity as well as permeability of free space $\epsilon_0 \approx 8.854 \cdot 10^{-12} \text{ As/Vm}$ and $\mu_0 = 4\pi \cdot 10^{-7} \text{ N/A}^2$ we determined the relative electric permittivity $\epsilon^r = \epsilon/\epsilon_0$ and relative magnetic permeability $\mu^r = \mu/\mu_0$, respectively.

Table 3: Material parameters used for the simulations of single crystal BaTiO₃, $[\hat{C}] = [\hat{\sigma}_c] = \frac{N}{\text{mm}^2}$, $[\hat{e}] = [\hat{P}_s] = \frac{C}{\text{m}^2}$, $[\hat{\epsilon}] = \frac{\text{mC}}{\text{kVm}}$, $[\hat{\epsilon}_s] = [\hat{\mu}^r] = [\hat{\epsilon}^r] = 1$, $[\hat{E}_c] = \frac{\text{kV}}{\text{mm}}$, $[\hat{\mu}] = \frac{N}{\text{kA}^2}$, see Zgonik et al. (1994). We roughly assumed the value of the coercive stress σ_c .

\hat{C}_{1111}	\hat{C}_{1122}	\hat{C}_{1133}	\hat{C}_{3333}	\hat{C}_{1212}	\hat{C}_{1313}	$\hat{e}_{11} (\hat{\epsilon}_{11}^r)$	$\hat{e}_{33} (\hat{\epsilon}_{33}^r)$
222000	108000	111000	151000	134000	61000	0.019 (2146)	0.000496 (56)
\hat{e}_{311}	\hat{e}_{333}	\hat{e}_{131}	$\hat{\mu}_{11} (\hat{\mu}_{11}^r)$	$\hat{\mu}_{33} (\hat{\mu}_{33}^r)$	\hat{E}_c	$\hat{\sigma}_c$	$\hat{\epsilon}_s$
-0.7	6.7	34.2	1.26 (1)	1.26 (1)	1.0	100	0.00834

In the initial state the orientations are distributed uniformly in the three-dimensional space to obtain an unpoled ferroelectric bulk material, in order to approximate a real material without a pre-polarization.

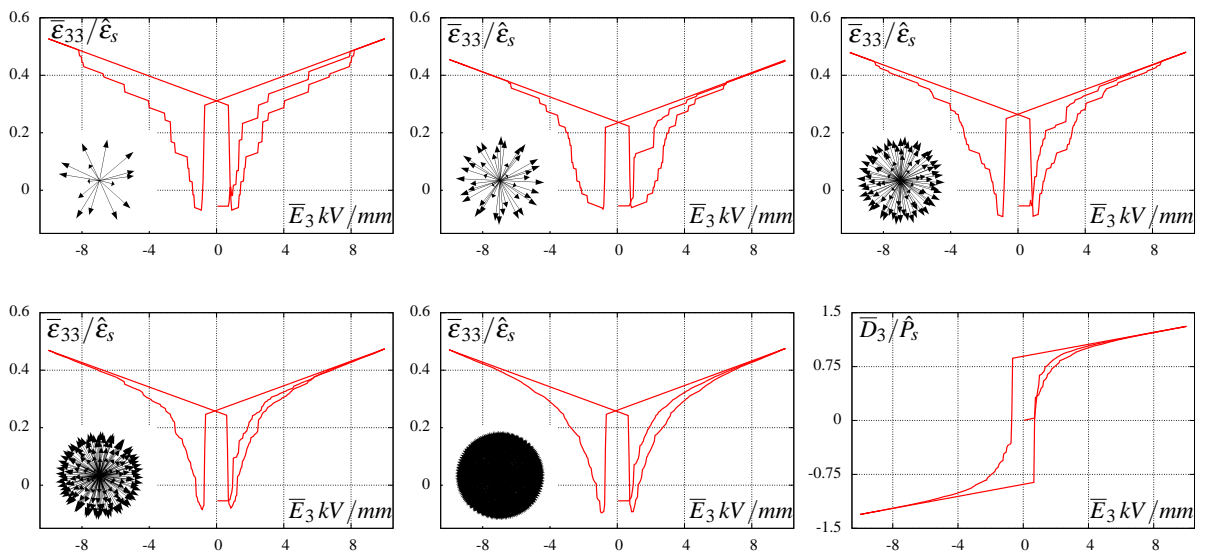


Figure 3: Macroscopic butterfly hysteresis loop using 15, 42, 92, 162 and 1002 orientations and a dielectric hysteresis loop for 1002 orientations.

Therefore, we make use of the construction of a geodesic dome (Fuller (1965)), whose surface is uniformly subdivided into multiple triangles, see for example Schröder et al. (2015a). Subsequently, the orientations, characterized by arrows, then point from the center of the geodesic sphere into the direction of a corresponding corner point of the surface triangles. By subdividing each triangular edge into multiple subsections, which is denoted by frequencies, the number of orientations can be increased. Typically, this construction principle yields 42, 92, 162 or 1002 orientations for a frequency of 2, 3, 4 or 10. Figures 3 shows the resulting butterfly hysteresis curves for an applied alternating vertical electric field \bar{E}_3 , with 15, 42, 92, 162 and 1002 orientations. Additionally, a dielectric hysteresis loop using 1002 orientations is depicted. The maximum applied electric field is increased to 10 kV/mm to ensure that each orientation is switched to its most efficient direction as well as to obtain a perfect symmetry of the hysteresis loops. As shown in Figure 3 the macroscopic response tends to smoother results for a larger number of orientations. Due to the application of an orientation distribution function for the spontaneous polarization directions and the accompanying spontaneous strains, we obtain an initial contraction of the material. This behavior is caused by the fact that the remanent strains of all orientations do not exactly cancel each other.

3.2 Ferroelectric Pressure Dependence

Based on the previous study of different numbers of orientations, we use 92 unit cells for the simulations in this section. To increase the electro-mechanical coupling a compressive stress is applied in the direction along the alternating electric field, see Figure 4. This is due to an enhancement of the stress-activated 90° ferroelastic switching, see e.g. Yen et al. (2008).

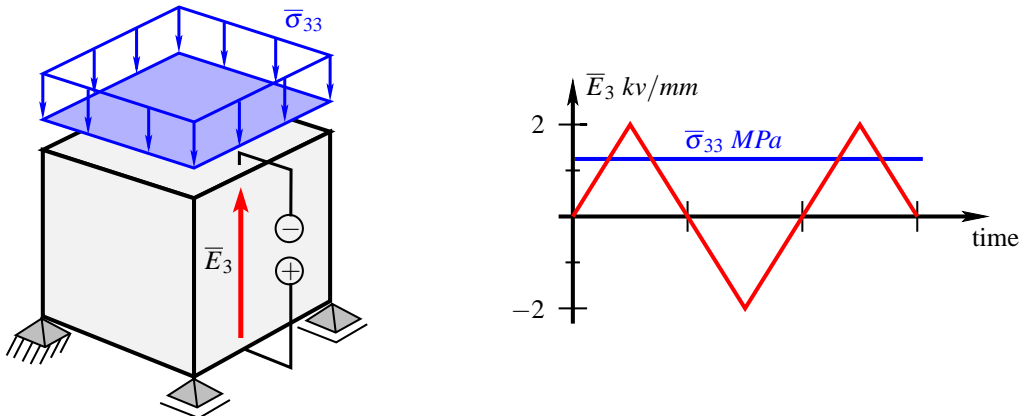


Figure 4: Macroscopic boundary value problem with applied electric field and compressive stresses.

The pressure dependence of a ferroelectric bulk material can be seen in the resulting hysteresis loops in Figure 5. Due to the applied stresses the material is compressed in the vertical direction and the remanent strains are shifted into a negative data region.

Comparing the different butterfly hysteresis loops, we observe a larger absolute value of the total strains, which can be achieved especially in low electric field ranges, where a distinct switching behavior occurs. On the other hand, the amplitudes of the dielectric hysteresis loop is narrowed for higher compressive stresses. Such a ferroelectric hysteretic response for applied uniaxial prestresses is also observed for soft PZT in Zhou et al. (2005).

3.3 Magneto-electric Coupling of Two-phase Composites

In this section we focus on the magneto-electric coupling of two-phase composites and take a closer look at the polarization state as well as the pressure dependence, which was in the previous sections investigated for a single-phase ferroelectric material. The magneto-electric coupling in composite materials is a strain-induced property and requires a distinct electro-mechanical coupling of the ferroelectric phase. Thus, the ME coupling can be increased by an improved electro-mechanical response of the electro-active phase, which can be achieved by poling of the ferroelectric matrix as well as by an applied compressive stress. To give an impression of the microscopic switching behavior, we consider a periodic \mathcal{NVE} on the microstructure, consisting of a ferroelectric matrix with a spherical piezomagnetic inclusion with 25% volume fraction, see Figure 6, which is driven by an alternating electric field in vertical direction. We assume 42 barium titanate unit cells at each integration point of the piezoelectric matrix, which are uniformly distributed in three dimensional space. In the following numerical example an applied alternating electric field yields alternating reorientations of the microscopic barium titanate

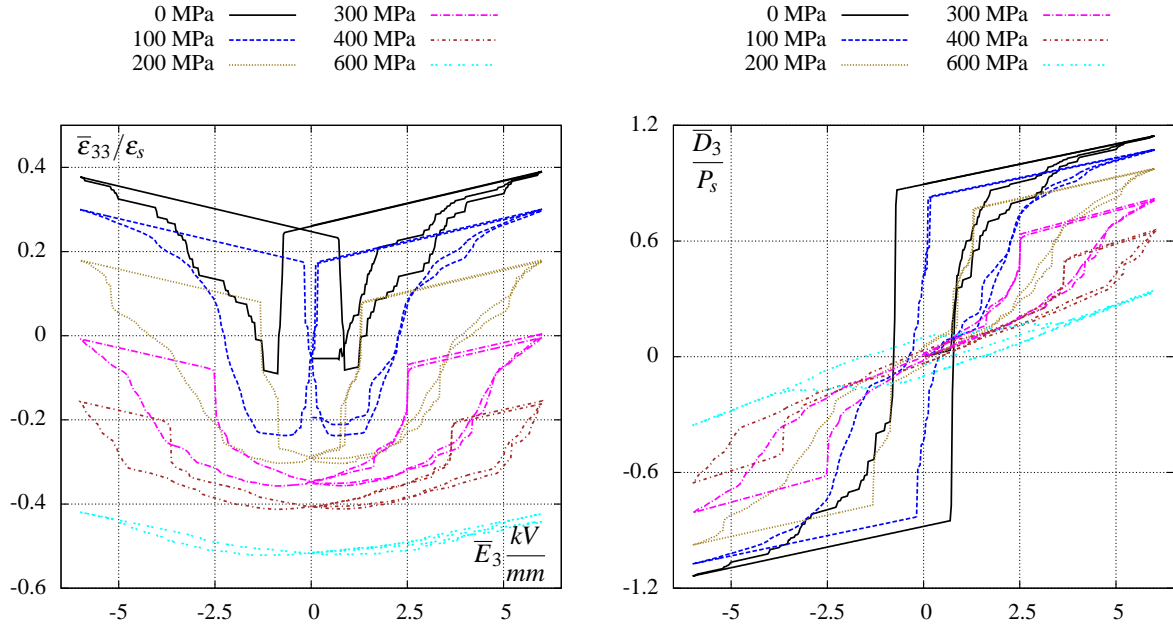


Figure 5: a) Butterfly hysteresis and b) dielectric hysteresis curves over an electric field \bar{E}_3 for different applied compressive stresses.

unit cells, which result in a non-linear behavior of the ME-coefficient depending on the polarization state of the ferroelectric matrix. To give an impression of the simulated microscopic switching behavior we apply a cycling electric field in vertical direction on the \mathcal{RVE} , see Figure 6a. In Figure 6b we show the distribution of E_3 and B_3 for a macroscopic loading $\bar{E}_3 = 2$ kV/mm at time t_4 . In order to demonstrate the polarization switching inside the \mathcal{RVE} , we have chosen two Gauss points, of which we illustrate the orientation distributions of the barium titanate unit cells for a sequence of macroscopic electric fields \bar{E}_3 for two distinguished points (1) and (2), see Figure 6c.

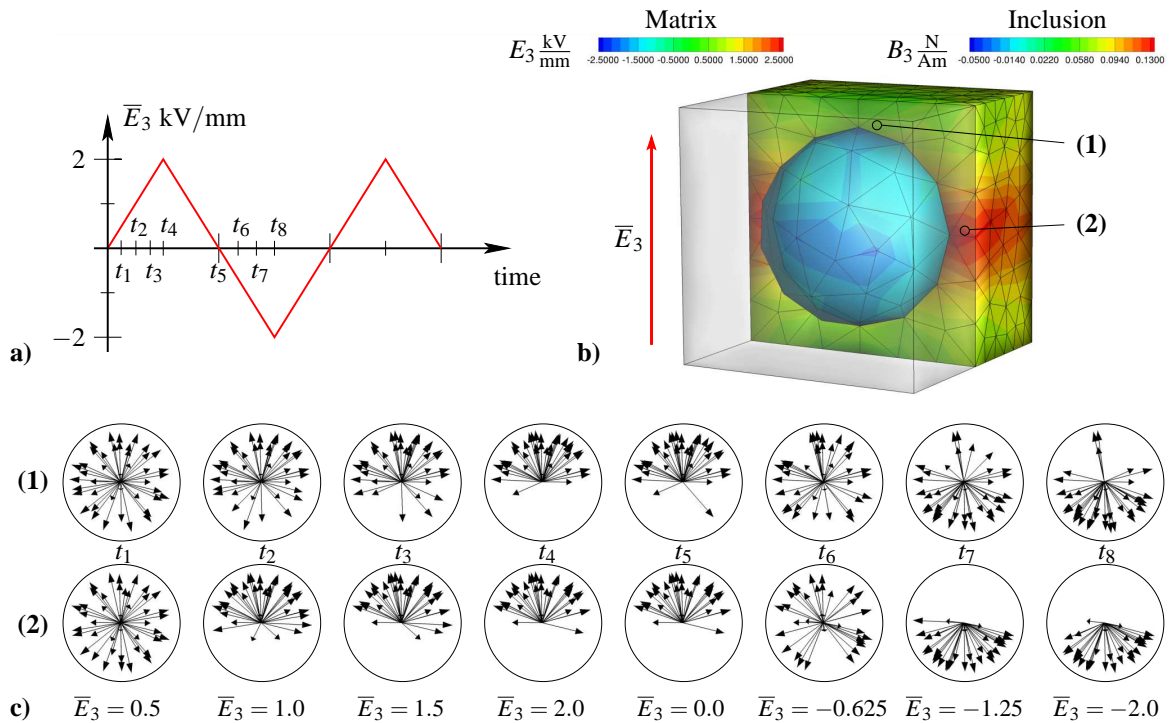


Figure 6: a) Cyclic loading of an alternating macroscopic electric field, b) \mathcal{RVE} and c) orientation distributions with distinguished points (1) and (2) at specific time steps.

The first point (1) is located above the magnetic inclusion, where the local electric field is smaller than the applied macroscopic field. The second point (2) is located at the right side of the inclusion, where a microscopic electric

field concentration (E_3) is observed in a horizontal area around the magnetic inclusion. For imaging the switching behavior the orientation distributions in both integration points are depicted at the eight points of time t_1 to t_8 , which focus on the loading process of the electric field in positive and negative direction. During the first 4 time steps t_1 to t_4 for an increased electric field we observe a switching of the orientations which then point into the direction of the applied field. When the electric field decreases to the maximum negative value, during the time steps t_5 to t_8 , a stepwise reorientation of the unit cells takes place. By comparing the behavior in both points we clearly see a different switching response due to the different local electric fields.

For a more precise prediction of the ME-coefficient we performed simulations with a refined finite element mesh of the \mathcal{RVE} s. Furthermore, we applied compressive stresses on the composite to investigate their influences on the ME-coefficient. The resulting hysteresis loops and the non-linear behavior of the ME-coefficients are depicted in Figure 7.

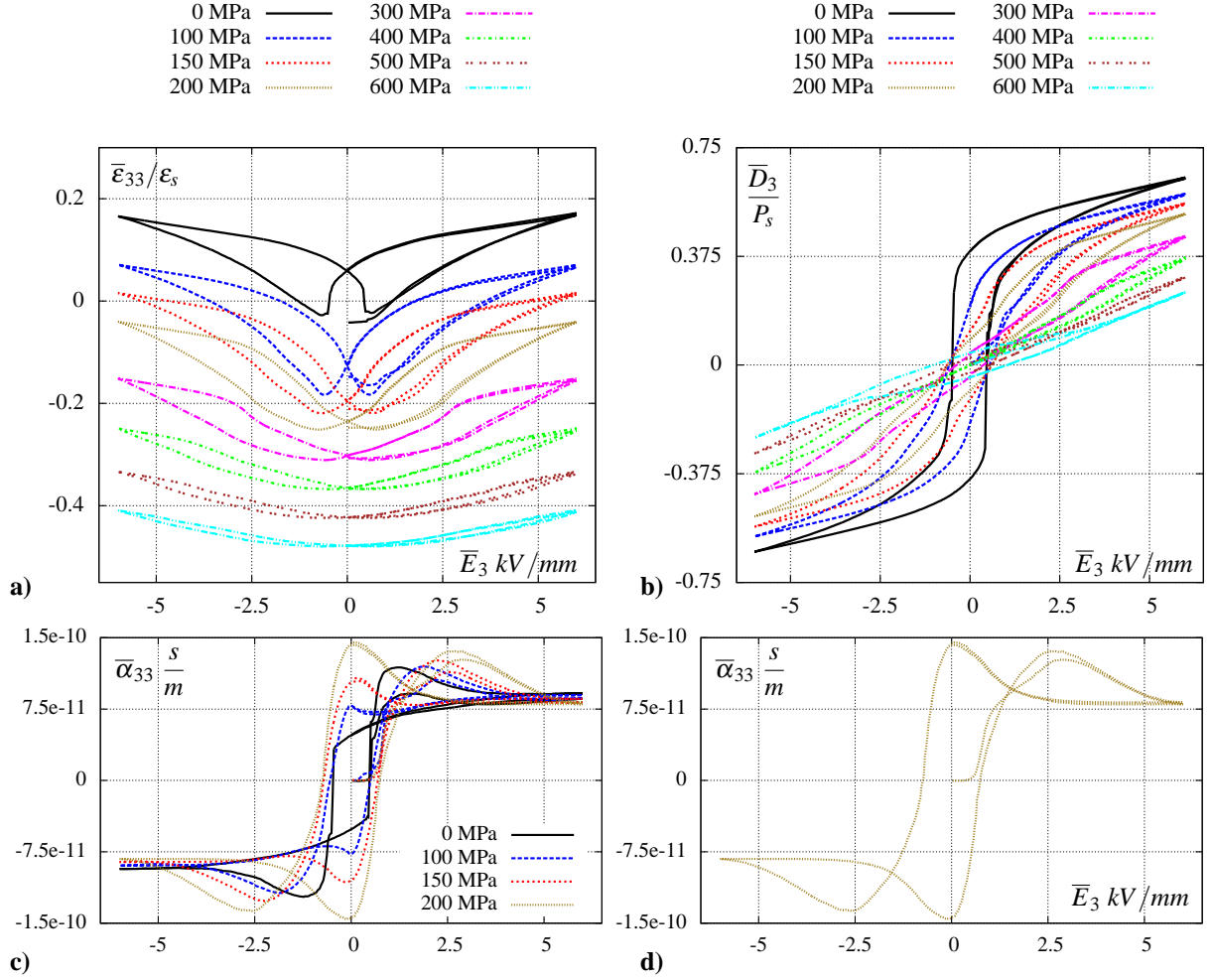


Figure 7: a) Effective response of the butterfly hysteresis loops, b) dielectric hysteresis, c) ME coefficient for applied stresses from 0 MPa to 200 MPa and d) ME coefficient for applied stresses of 200 MPa.

We observe a strong dependency of the transferred strains from the electric matrix to the magnetic inclusion on the ME coefficient. The magnitude of the magneto-electric coupling is based on the incremental change of the electric butterfly hysteresis curve. Here we observe a saturation of the ME-coefficient under high electric fields. When the electric field loading is removed, a remanent ME-coefficient remains, which is in the case of no compressive stresses approximately half to the one predicted with purely linear piezoelectric and piezomagnetic material models with assumed idealized polarization and magnetization. The modified electro-mechanical behavior in case of applied compressive stresses affects the magneto-electric coupling in a positive manner, see Figure 7c. At a compressive stress of 200 MPa the ME-coefficient at remanent polarization is raised up to $\bar{\alpha}_{33}(\bar{\sigma}_{33} = 200MPa) = 1.423 \cdot 10^{-10}$ s/m and is 304.1 % larger than the coupling coefficient at an unstressed state ($\bar{\alpha}_{33}(\bar{\sigma}_{33} = 0 MPa) = 0.4709 \cdot 10^{-11}$ s/m). The performed simulations of the ME coefficients are not adjusted to experimental measurements and are purely predictions of the used material models. However, the authors would assume a decrease of the ME coefficient for increasing applied compressive stresses. This material behavior is due to the complexity of the microscopic interactions an open question, which will be investigated in a future work, where we will compare the simulated results with experimental measurements.

3.4 Influence of the Microscopic Morphology on ME Coefficients

As already demonstrated in Figure 6 the heterogeneous microstructure and the resulting inhomogeneous distribution of the local electric fields play a significant role on the local polarization states. Regions inside the microstructure with low electric field distributions show accordingly small electro-mechanical properties, which decreases the strain-induced magneto-electric coupling. To investigate the influence of the microscopic morphology on the ME-coefficient we performed 25 simulations with composites, consisting of a piezoelectric matrix and different ellipsoidal piezomagnetic inclusions with varying volume fractions. Here, we restricted the simulations to two-dimensional boundary value problems and purely transversely isotropic linear material models. The used material parameters for polycrystalline barium titanate and cobalt ferrite are listed in Table 4. Here it has to be emphasized, that we consider non-conductive magnetic inclusion. In all simulations a macroscopic electric field of 2 kV/mm in vertical direction is applied and periodic boundary conditions are used on the $\mathcal{R}^V \mathcal{E}$.

Table 4: Material parameters for polycrystal barium titanate and cobalt ferrite, see Bechmann (1956); Stevens et al. (1956); Murthy (1983); Lee et al. (2005); Labusch et al. (2014); Schröder et al. (2015a).

Modulus	Unit	BaTiO ₃	CoFe ₂ O ₄	Modulus	Unit	BaTiO ₃	CoFe ₂ O ₄
C_{11}	$\frac{N}{mm^2}$	$16.6 \cdot 10^4$	$21.21 \cdot 10^4$	$\epsilon_{11} (\epsilon_{11}^r)$	$\frac{mC}{kVm}$	$112 \cdot 10^{-4} (1265)$	$0.80 \cdot 10^{-4} (9)$
C_{12}	$\frac{N}{mm^2}$	$7.7 \cdot 10^4$	$7.45 \cdot 10^4$	$\epsilon_{33} (\epsilon_{33}^r)$	$\frac{mC}{kVm}$	$126 \cdot 10^{-4} (1423)$	$0.93 \cdot 10^{-4} (11)$
C_{13}	$\frac{N}{mm^2}$	$7.8 \cdot 10^4$	$7.45 \cdot 10^4$	q_{31}	$\frac{N}{kAmm}$	0.0	580.3
C_{33}	$\frac{N}{mm^2}$	$16.2 \cdot 10^4$	$21.21 \cdot 10^4$	q_{33}	$\frac{N}{kAmm}$	0.0	-699.7
C_{44}	$\frac{N}{mm^2}$	$4.3 \cdot 10^4$	$6.88 \cdot 10^4$	q_{15}	$\frac{N}{kAmm}$	0.0	550.0
e_{31}	$\frac{C}{m^2}$	-4.4	0.0	$\mu_{11} (\mu_{11}^r)$	$\frac{N}{kA^2}$	1.26 (1.003)	157.0 (124.9)
e_{33}	$\frac{C}{m^2}$	18.6	0.0	$\mu_{33} (\mu_{33}^r)$	$\frac{N}{kA^2}$	1.26 (1.003)	157.0 (124.9)
e_{15}	$\frac{C}{m^2}$	11.6	0.0				

Figure 8 shows three example microstructures with different inclusion geometries but equal volume fractions. The longitudinal expansions of the ellipsoids with varying volume fractions is kept constant to enable a comparison with the different microstructures. Figure 8 also depicts the electric field distribution E_2 of the composites.

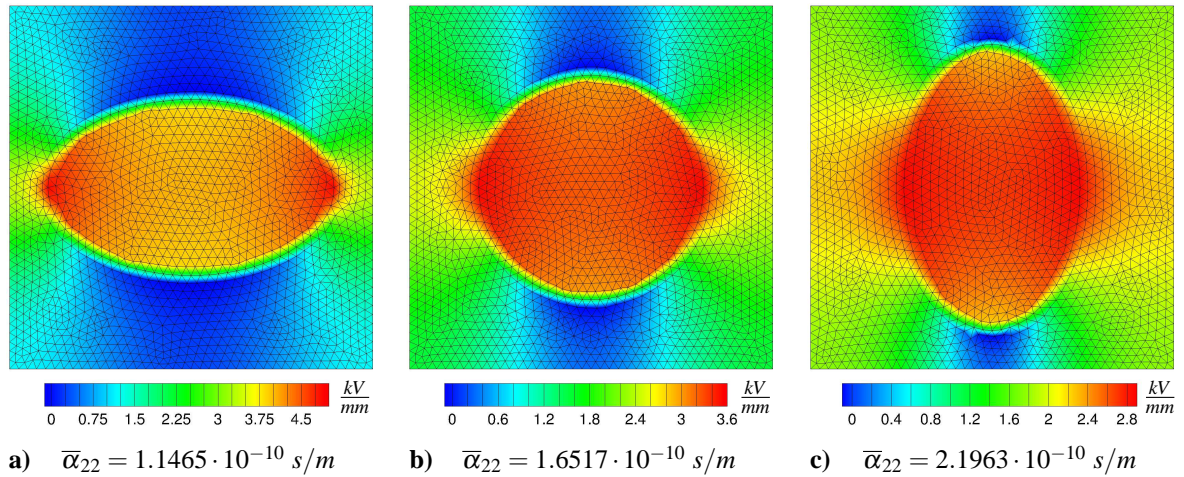


Figure 8: Electric field distribution E_2 for three example microstructures with 30 % inclusion volume fraction.

We can clearly observe, that due to the different electric permittivity of the magnetic inclusion concentrations of the electric fields occur at the left and right boundary of the inclusions. Simultaneously, very low microscopic electric fields, in comparison with the applied macroscopic field, are present at the vertical boundaries. For a high magneto-electric coupling the electro-mechanical properties of the matrix in the regions of the interphase between both constituents should also be enhanced, which is the case for ellipsoidal inclusions aligned along the direction of the applied electric field. As a consequence the ME-coefficient for the three composites raised from $\bar{\alpha}_{22} = 1.1465 \cdot 10^{-10} \text{ s/m}$ for a) over $\bar{\alpha}_{22} = 1.6517 \cdot 10^{-10} \text{ s/m}$ for b) to $\bar{\alpha}_{22} = 2.1963 \cdot 10^{-10} \text{ s/m}$ for c).

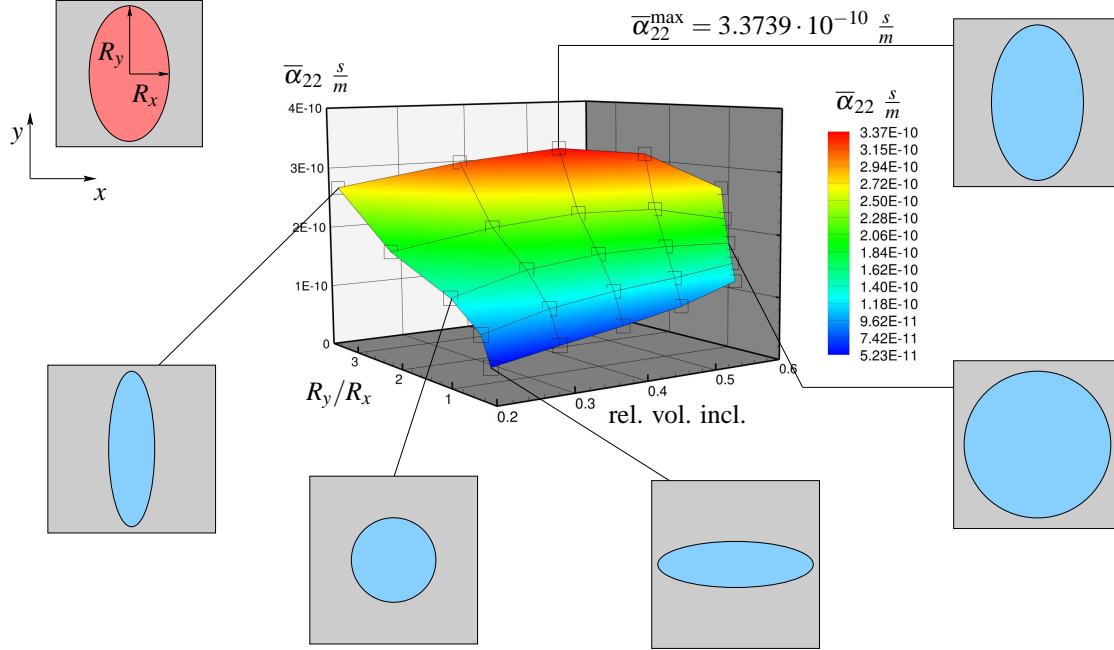


Figure 9: Three-dimensional visualization of the ME-coefficients for different inclusion geometries and volume fractions.

A visualization of the ME-coefficients of all considered microstructures is given in Figure 9. The resulting ME-coefficients are plotted against the inclusion volume fraction and the ratio between the horizontal and vertical radius of the ellipsoidal inclusion, which yield a three-dimensional plot, where the highest point of the surface describes the maximum ME-coefficient. Taking a closer look at Figure 9 we observe, that for a circular inclusion the best ME value is obtained for 50 % volume fraction of both phases. As demonstrated in Figure 8 the ME coupling can be increased by changing the inclusion shape to ellipsoid aligned along the direction of the applied field. Thus, the highest ME-coefficient $\bar{\alpha}_{22} = 3.3739 \cdot 10^{-10} \text{ s/m}$ is obtained for a microstructure with a vertical ellipsoidal inclusion with 40 % volume fraction.

4 Conclusion

In this contribution, we proposed a two-scale homogenization approach for magneto-electro-mechanically coupled boundary value problems. The procedure was implemented into the FE²-method, which allows for the consideration of attached microscopic representative volume elements to compute the macroscopic boundary value problem. The main focus is on the determination of the magneto-electric coefficient and consideration of the influences of applied stresses and microscopic morphologies on the ME coupling. Numerical simulations demonstrate the enhancement of the ME-coefficient under compressive stresses and for specific shapes of the magnetic inclusions. To further improve the prediction of the effective properties, we inspected a ferroelectric pre-polarization process by considering the microscopic ferroelectroelastic switching behavior. In this contribution we have neglected any conductivity of the magnetic inclusion considering only the net (= high frequency) dielectric constant. The more realistic case of low but finite conductivity is planned for future work. In future developments we will more precisely simulate the magnetostrictive response by implementing a non-linear dissipative material model.

Acknowledgement

We gratefully acknowledge the financial support of the German Research Foundation (DFG) in the framework of the research unit 1509 “Ferroic Functional Materials – Multiscale Modeling and Experimental Characterization”, project 1 SCHR 570/12-1, project 2 (LU 729/12) and project 3 (KE 1849/2-2).

References

- Arockiarajan, A.; Sivakumar, S.; Sansour, C.: A thermodynamically motivated model for ferroelectric ceramics with grain boundary effects. *Smart Materials and Structures*, 19(1), (2010), 015008.
- Astrov, D.: Magnetolectric effect in chromium oxide. *Journal of Experimental and Theoretical Physics*, 40, (1961), 1035–1041.
- Avakian, A.; Gellmann, R.; Ricoeur, A.: Nonlinear modeling and finite element simulation of magnetolectric coupling and residual stress in multiferroic composites. *Acta Mechanica*, 226, (2015), 2789–2806.
- Bechmann, R.: Elastic, piezoelectric, and dielectric constants of polarized barium titanate ceramics and some applications of the piezoelectric equations. *The Journal of the Acoustical Society of America*, 28, (1956), 347–350.
- Bibes, M.; Barthélémy, A.: Multiferroics: Towards a magnetolectric memory. *Nature Materials*, 7, 6, (2008), 425–426.
- Crottaz, O.; Rivera, J.-P.; Revaz, B.; Schmid, H.: Magnetolectric effect of $Mn_3B_7O_{13}I$ boracite. *Ferroelectrics*, 204, (1997), 125–133.
- Eerenstein, W.; Mathur, N. D.; Scott, J. F.: Multiferroic and magnetolectric materials. *Nature*, 442, 7104, (2006), 759–765.
- Fiebig, M.: Revival of the magnetolectric effect. *Journal of Physics D: Applied Physics*, 38, (2005), R123–R152.
- Fuller, R.: Geodesic Structures (August 1965).
- Geers, M. G. D.; Kouznetsova, V. G.; Brekelmans, W. A. M.: Multi-scale computational homogenization: Trends and challenges. *Journal of Computational and Applied Mathematics*, 234, 7, (2010), 2175–2182, fourth International Conference on Advanced Computational Methods in Engineering (ACOMEN 2008).
- Hill, N.: Why are there so few magnetic ferroelectrics? *The Journal of Physical Chemistry B*, 104, (2000), 6694–6709.
- Hill, R.: Elastic properties of reinforced solids – some theoretical principles. *Journal of the Mechanics and Physics of Solids*, 11, (1963), 357–372.
- Huber, J.; Fleck, N.; Landis, C.; McMeeking, R.: A constitutive model for ferroelectric polycrystals. *Journal of the Mechanics and Physics of Solids*, 47, (1999), 1663–1697.
- Hwang, S.; Lynch, C.; McMeeking, R.: Ferroelectric/ferroelastic interaction and a polarization switching model. *Acta metall. mater.*, 43, (1995), 2073–2084.
- Kamlah, M.: Ferroelectric and ferroelastic piezoceramics - modeling of electromechanical hysteresis phenomena. *Continuum Mechanics and Thermodynamics*, 13, (2001), 219–268.
- Kamlah, M.; Liskowsky, A.; McMeeking, R.; Balke, H.: Finite element simulation of a polycrystalline ferroelectric based on a multidomain single crystal switching model. *International Journal of Solids and Structures*, 42, (2005), 2949–2964.
- Keip, M.-A.: *Modeling of Electro-Mechanically Coupled Materials on Multiple Scales*. Ph.D. thesis, University of Duisburg-Essen (2012).
- Keip, M.-A.; Schröder, J.: A ferroelectric and ferroelastic microscopic switching criterion for tetragonal ferroelectrics. *Proceedings in Applied Mathematics and Mechanics*, 11, 1, (2011), 475–476.
- Keip, M.-A.; Schröder, J.: On the modeling of microscopic switching phenomena in tetragonal ferroelectric materials. In: *Proceedings of the 19th International Conference on Computer Methods in Mechanics, CMM 2011*, Warschau, Polen (Mai, 9-12 2011).
- Keip, M.-A.; Steinmann, P.; Schröder, J.: Two-scale computational homogenization of electro-elasticity at finite strains. *Computer Methods in Applied Mechanics and Engineering*, 278, (2014), 62–79.
- Kessler, H.; Balke, H.: On the local and average energy release in polarization switching phenomena. *Journal of the Mechanics and Physics of Solids*, 49, (2001), 953–978.

- Klinkel, S.: A phenomenological constitutive model for ferroelastic and ferroelectric hysteresis effects in ferroelectric ceramics. *International Journal of Solids and Structures*, 43, (2006), 7197–7222.
- Labusch, M.; Etier, M.; Lupascu, D.; Schröder, J.; Keip, M.-A.: Product properties of a two-phase magneto-electric composite: Synthesis and numerical modeling. *Computational Mechanics*, 54, (2014), 71–83.
- Lee, J. S.; Boyd, J. G.; Lagoudas, D. C.: Effective properties of three-phase electro-magneto-elastic composites. *International Journal Of Engineering Science*, 43, 10, (2005), 790–825.
- Li, Q.; Ricoeur, A.; Enderlein, M.; Kuna, M.: Evaluation of electromechanical coupling effect by microstructural modeling of domain switching in ferroelectrics. *Mechanics Research Communications*, 37, (2010), 332–336.
- Mandel, J.; Dantu, P.: Contribution à l'étude théorique et expérimentale du coefficient d'élasticité d'un milieu hétérogène mais statistiquement homogène. *Annales des Ponts et Chaussées*.
- McMeeking, R.; Hwang, S.: On the potential energy of a piezoelectric inclusion and the criterion for ferroelectric switching. *Ferroelectrics*, 200, (1997), 151–173.
- McMeeking, R.; Landis, C.: A phenomenological multi-axial constitutive law for switching in polycrystalline ferroelectric ceramics. *International Journal of Engineering Science*, 40, (2002), 1553–1577.
- Miehe, C.; Bayreuther, C.: On multiscale FE analyses of heterogeneous structures: from homogenization to multi-grid solvers. *International Journal For Numerical Methods In Engineering*, 71, (2007), 1135–1180.
- Miehe, C.; Koch, A.: Computational micro-to-macro transitions of discretized microstructures undergoing small strains. *Archive of Applied Mechanics*, 72, 4, (2002), 300–317.
- Miehe, C.; Rosato, D.: A rate-dependent incremental variational formulation of ferroelectricity. *International Journal of Engineering Science*, 49, (2011), 466–496.
- Miehe, C.; Rosato, D.; Kiefer, B.: Variational principles in dissipative electro-magneto-mechanics: A framework for the macro-modeling of functional materials. *International Journal for Numerical Methods in Engineering*, 86, 10, (2011), 1225–1276.
- Murthy, S.: Delta-e effect in co-zn ferrites. *Physica Status Solidi A-Applied Research*, 80, (1983), K161–K165.
- Nan, C.-W.: Magnetoelectric effect in composites of piezoelectric and piezomagnetic phases. *Phys. Rev. B*, 50, (1994), 6082–6088.
- Rivera, J.-P.: On definitions, units, measurements, tensor forms of the linear magnetoelectric effect and on a new dynamic method applied to cr-cl boracite. *Ferroelectrics*, 161, (1994), 165–180.
- Rivera, J.-P.; Schmid, H.: On the birefringence of magnetoelectric bifeo₃. *Ferroelectrics*, 204, (1997), 23–33.
- Schrade, D.; Mueller, R.; Xu, B.; Gross, D.: Domain evolution in ferroelectric materials: A continuum phase field model and finite element implementation. *Computer methods in applied mechanics and engineering*, 196, (2007), 4365–4374.
- Schrade, D.; Müller, R.; Gross, D.; Keip, M.-A.; Thai, H.; Schröder, J.: An invariant formulation for phase field models in ferroelectrics. *International Journal of Solids and Structures*, 51, 11, (2014), 2144–2156.
- Schröder, J.: Derivation of the localization and homogenization conditions for electro-mechanically coupled problems. *Computational Materials Science*, 46, 3, (2009), 595–599.
- Schröder, J.; Gross, D.: Invariant formulation of the electromechanical enthalpy function of transversely isotropic piezoelectric materials. *Archive of Applied Mechanics*, 73, (2004), 533–552.
- Schröder, J.; Keip, M.-A.: Two-scale homogenization of electromechanically coupled boundary value problems. *Computational Mechanics*, 50, (2012), 229–244.
- Schröder, J.; Labusch, M.; Keip, M.-A.: Algorithmic two-scale transition for magneto-electro-mechanically coupled problems - fe²-scheme: Localization and homogenization. *Computer Methods in Applied Mechanics and Engineering*, (submitted), . in preparation.
- Schröder, J.; Labusch, M.; Keip, M.-A.; Kiefer, B.; Brands, D.; Lupascu, D.: Computation of non-linear magneto-electric product properties of 0-3 composites. *GAMM-Mitteilungen*, 38(1), (2015b), 1–8.

- Schröder, J.; Romanowski, H.: A thermodynamically consistent mesoscopic model for transversely isotropic ferroelectric ceramics in a coordinate-invariant setting. *Archive of Applied Mechanics*, 74, 11-12, (2005), 863–877.
- Spaldin, N.; Fiebig, M.: The Renaissance of Magnetoelectric Multiferroics. *Science*, 309, (2005), 391–392.
- Stevens, D.; Schweinler, H.; Sturm, W.; Sonder, E.: The magnetic susceptibility of barium titanate. *Solid State Division Semiannual Progress Report*, 30, (1956), 13–14.
- Vaz, C.; Hoffman, J.; Ahn, C.; Ramesh, R.: Magnetoelectric coupling effects in multiferroic complex oxide composite structures. *Advanced Materials*, 22, (2010), 2900–2918.
- Yen, J.; Shu, Y.; Shieh, J.; Yeh, J.: A study of electromechanical switching in ferroelectric single crystals. *Journal of the Mechanics and Physics of Solids*, 56, (2008), 2117–2135.
- Zäh, D.; Miehe, C.: Computational homogenization in dissipative electro-mechanics of functional materials. *Computer Methods in Applied Mechanics and Engineering*, 267, (2013), 487–510.
- Zgonik, M.; Bernasconi, P.; Duelli, M.; Schlessler, R.; Günter, P.: Dielectric, elastic, piezoelectric, electro-optic, and elasto-optic tensors of BaTiO₃ crystals. *Physical Review B*, 50(9), (1994), 5941–5949.
- Zhang, W.; Bhattacharya, K.: A computational model of ferroelectric domains. Part I: model formulation and domain switching. *Acta Materialia*, 53, 1, (2005), 185–198.
- Zhou, D.; Kamlah, M.; Munz, D.: Effects of uniaxial prestress on the ferroelectric hysteretic response of soft pzt. *Journal of the European Ceramic Society*, 25, (2005), 425–432.

Address: M.Sc. Matthias Labusch, Fakultät für Ingenieurwissenschaften, Institut für Mechanik, Abteilung Bauwissenschaften, Universitätsstraße 15, 45141 Essen
email: matthias.labusch@uni-due.de